IEEE Access
Multidisciplinary | Rapid Review | Open Access Journal

Received January 11, 2022, accepted February 3, 2022, date of publication February 9, 2022, date of current version February 17, 2022.

Digital Object Identifier 10.1109/ACCESS.2022.3150393

Investigation of the Effects of the Pole Shoe Geometry on the IPM T-LSM Features: Application to Free Piston Engines

AMAL SOUISSI, IMEN ABDENNADHER, AND AHMED MASMOUDI, (Senior Member, IEEE)
Research Laboratory on Renewable Energies and Electric Vehicles (RELEV), ENIS, University of Sfax, Sfax 3038, Tunisia
Corresponding author: Ahmed Masmoudi (a.masmoudi@enis.rnu.tn)

This work was supported by the University of Sfax, Tunisia.

ABSTRACT The paper is aimed at an analytical approach dedicated to the investigation of the effects of the pole shoe geometry on the no-load flux features of inner permanent magnet tubular-linear synchronous machines (IPM T-LSMs). It considers the most common geometries: (i) rectangular pole shoes, and (ii) trapezoidal pole shoes. The proposed approach combines two analytical models which are the magnetic equivalent circuit (MEC) and the permeance function. First, a basic MEC of an elementary part of the machine is considered to predict a preliminary air gap flux density trapezoidal waveform. Then, the accuracy of the proposed approach is enhanced by the incorporation of a mover permeance function that accounts for the PM spoke-type arrangement. The proposed approach is applied to the investigation of the impact of the mover pole shoe shape on the air gap flux density. The developed pole shoe sizing procedure makes it possible the selection of an IPM T-LSM with an appropriate mover geometry for which an investigation of the no- and on-load features is carried out by finite element analysis. The prototyping of the selected topology enables the experimental validation of the back-EMF and the load characteristic.

INDEX TERMS Tubular-linear synchronous machines, inner permanent magnets, mover pole shoes, magnetic equivalent circuit, mover permeance function, no-load air gap flux density, back-EMF, cogging force, finite element analysis.

I. INTRODUCTION

Linear machines have been and continue to be viable candidates in several industrial fields where they exhibit higher performance than their rotating counterparts. They are integrated in wave energy conversion systems [1]–[4], Maglev trains [5]–[7], ropeless elevators [8], [9], electromagnetic suspensions [10], [11], and free piston engines [12]–[15].

The latter are suitably-adapted to equip series hybrid electric vehicles (HEVs) where the internal combustion engine (ICE) is no longer involved in driving the wheels. Its role is limited to a prime mover of the generator. Accounting for the oscillating motion in ICE chambers, a the mover of a linear generator can be directly coupled to the piston without a linear-to-rotating motion conversion, yielding the so-called ''direct-drive'' concepts. These are reputed by their improved energy efficiency compared to conventional systems where the ICE is coupled to a rotating generator.

The associate editor coordinating the review of this manuscript and approving it for publication was Guillaume Parent.

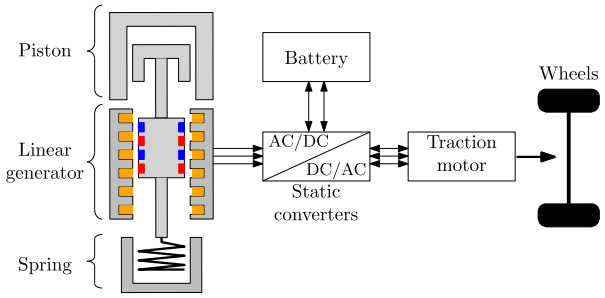

FIGURE 1. Series hybrid propulsion system equipped with a free piston engine.

Fig. 1 illustrates the scheme of a series hybrid propulsion system equipped with a free piston engine [16]. Different topologies of free piston engines have been presented in [17].

Further improvement of the energy efficiency could be gained through the selection of permanent magnet (PM) linear synchronous machines rather than switched reluctance or

induction ones. PM linear synchronous machines exhibit the highest force density when powerful magnets are used. Much interest is presently given to the design [18], sizing [19] and optimization of PM linear synchronous machines. Among the design aspects, one can distinguish the PM arrangement with emphasis on the three following ones: (i) surface-mounted PMs, (ii) inner PMs, and (iii) quasi-*Halbach* PMs.

The air gap flux density is one of the most targeted features [20]. Its prediction has been the subject of different analytical, numerical, and combined analytical-numerical approaches. It is commonly known that finite element analysis (FEA)-based numerical models are reputed by their high accuracy in predicting the air gap flux density. However, they incorporate time-consuming procedures especially when three dimensional (3D) models are considered. Even in two dimensional (2D) models, a large CPU time is required for sizing and optimization procedures. Hence, much attention is paid to the development of analytical models based on:

1) vectorial or scalar potential formulations (V-SPF) [21],
2) magnetic equivalent circuits (MEC) [22].

Both modelling approaches are reputed by their low CPU time allied to an acceptable accuracy.

Referring to the works reported in the literature, the V-SPF models provide a high accuracy in the case of slotless machines [23], [24]. Their application to the sizing [25] and optimization [26], [27] of electric machines has led to a reasonable results which are validated by experiments.

In the case of slotted machines, the most common V-SPF models are based on the subdomain approach [28]–[33]. These have led to complicated formulations that take into account the characteristic of the different domains. Moreover, their resolution considers complicated boundary conditions expressed in terms of the magnetic potential and field.

The modelling of slotted machines could be also achieved using the MEC models. These latter have been formulated in several forms depending on the considered assumptions and the features under investigations, yielding a simplicity-accuracy tradeoff. For instance, a simple MEC model can be established assuming infinite length machines and infinite iron permeability [34], [35]. However, more representative MECs could be derived by discarding the previous assumptions. The incorporation of the rotor/mover position in the MEC is of interest as it extends the investigation to the machine time-varying features [19], [36]. Further accuracy could be gained through a 3D discretization of the machine geometry into elementary MECs, allied to an increase of the CPU time required for the MEC resolution [37].

In light of the above literature review, it is quite commonly believed that a given level of expertise is required in order to account for the major involved electromagnetic phenomena, in an attempt to reach representative analytical models. However, this is usually achieved to the detriment of their simplicity.

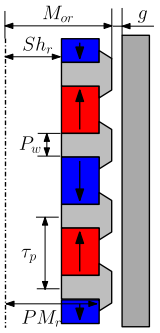

FIGURE 2. Basic concept of the IPM T-LSM under study.

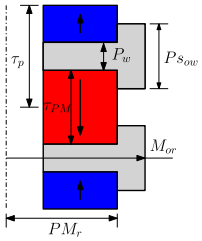

FIGURE 3. Rectangular pole shoe geometrical characterization.

Referring to [25], it has been found that the shape of the mover pole without pole shoes of IPM T-LSMs, greatly influences the harmonic content of the flux density spatial repartition. In this work, an affordable analytical approach is introduced in order to investigate the impact of the pole shoe geometry on the air gap flux density. This has been achieved considering rectangular and trapezoidal pole shoes and assuming a slotless stator.

II. POLE SHOE GEOMETRY DESCRIPTION

Fig. 2 illustrate the basic concept of the IPM T-LSM topology under study where the main geometrical parameters are identified.

Trapezoidal pole shoes have arbitrary considered in the basic concept shown in Fig. 2. Referring to the literature, the pole shoes have different geometry. This work treats the most common geometries, such that: (i) rectangular pole shoes, and (ii) trapezoidal pole shoes. These are characterized hereunder.

A. RECTANGULAR POLE SHOES

Fig. 3 shows a mover pole pair with rectangular pole shoe. Let us define ratios R_{pw} and R_{psw} characterizing the rectangular pole geometry, as follows:

$$\begin{cases} R_{pw} = \dfrac{P_w}{\tau_p} \\ R_{psw} = \dfrac{P_{sow} - P_w}{\tau_{PM}} \end{cases} \tag{1}$$

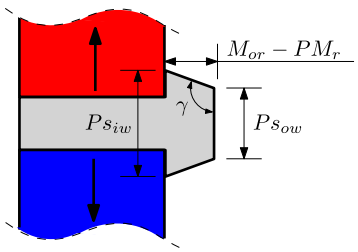

FIGURE 4. Trapezoidal pole shoe geometrical characterization.

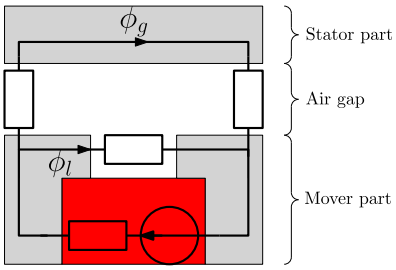

FIGURE 5. Magnetic equivalent circuit of an elementary part of the machine.

where the geometrical parameters P_w, τ_p, P_{sow}, and τ_{PM} are defined in Fig. 3.

B. TRAPEZOIDAL POLE SHOES

Fig. 4 shows a mover pole pair with trapezoidal pole shoe. It is characterized by the pole shoe angle γ.

III. ANALYTICAL APPROACH AIMED AT THE INVESTIGATION OF THE MOVER POLE GEOMETRY

A. METHODOLOGY

The goal of the proposed approach is to predict the air gap flux density taking into account the different effects resulting from the mover geometry variation. The developed approach consists in two main steps which are described as follows:

1) the prediction of the air gap flux density maximum value. To do so, a MEC, of an elementary part of the machine characterized by one pole length, is considered as shown in Fig. 5.
2) the formulation of the spatial repartition of the flux density considering the following sub-steps:
   - a preliminary trapezoidal waveform having a constant region characterized by a value equal to the one predicted in the first step (B_{max}) and an opening equal to the pole span, as illustrated in Fig. 6(b),
   - a mover permeance function modulating the preliminary trapezoidal waveform characterised by the geometrical parameters of the mover pole shoe, as shown in Fig. 6(c).

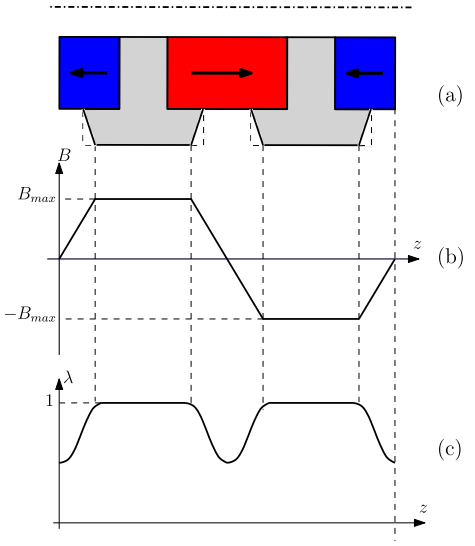

FIGURE 6. Air gap flux density waveform assessment. **Legend:** (a) mover geometry, (b) trapezoidal air gap flux density, and (c) layout of the mover permeance function.

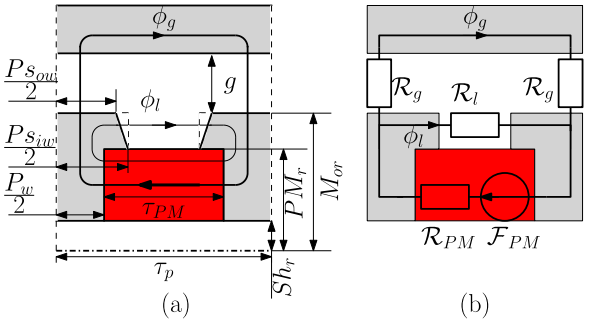

FIGURE 7. Elementary part of the IPM T-LSM. **Legend:** (a) flux loops and geometrical parameters, (b) magnetic equivalent circuit.

B. ANALYTICAL FORMULATION

1) PREDICTION OF THE AIR GAP FLUX DENSITY MAXIMUM VALUE

An elementary section of the IPM T-LSM, consisting in a single pole magnetic circuit, is shown in Fig. 7(a). For the sake of simplicity, the following assumptions have been adopted:

- a slotless stator magnetic circuit,
- an infinite iron magnetic permeability compared to the air and PM ones.

Accounting for the above assumptions, a MEC of the machine elementary part has been established as shown in Fig. 7(b), where $\mathcal{F}_{PM}$ is the PM magnetomotive force, and where $\mathcal{R}_g$, $\mathcal{R}_{PM}$, and $\mathcal{R}_l$ are the reluctances of the air gap, the PM, and the inter pole shoe regions, respectively.

The above-described MMF and reluctances are expressed as follows:

$$\begin{cases} \mathcal{F}_{PM} = \dfrac{B_r \tau_{PM}}{\mu_0 \mu_{PM}} \\ \mathcal{R}_g = \dfrac{ln(1+\frac{g}{M_{or}})}{\mu_0 \pi P s_{ow}} \\ \mathcal{R}_{PM} = \dfrac{\tau_{PM}}{\mu_0 \mu_{PM} \pi (PM_r^2 - Sh_r^2)} \\ \mathcal{R}_l = \dfrac{l_l}{\mu_0 \pi (M_{or}^2 - PM_r^2)} \end{cases} \tag{2}$$

where B_r and μ_{PM} are the PM magnetic remanence and relative permeability, respectively, and where l_l is the mean length characterizing the leakage flux ϕ_l path.

It is to be noted that l_l is mainly dependent on the trapezoidal pole shoe geometry. In the case of rectangular shape (interrupted lines in Fig. 7(a)), l_l is equal to $\tau_p - Ps_{ow}$.

The resolution of the MEC shown in Fig. 7(b) has led to the prediction of the main flux ϕ_g and the leakage one ϕ_l, as:

$$\begin{cases} \phi_g = \dfrac{\mathcal{F}_{PM}}{2\mathcal{R}_g(\frac{\mathcal{R}_{PM}}{\mathcal{R}_l}+1)+\mathcal{R}_{PM}} \\ \phi_l = \dfrac{\mathcal{F}_{PM}}{\mathcal{R}_l(\frac{\mathcal{R}_{PM}}{2\mathcal{R}_g}+1)+\mathcal{R}_{PM}} \end{cases} \tag{3}$$

Then, B_{max} can be expressed as follows:

$$B_{max} = \frac{\phi_g}{S_g} \tag{4}$$

where S_g is the air gap surface facing the half of a pole shoe, as:

$$S_g = 2\pi(M_{or} + \frac{g}{2})\frac{Ps_{ow}}{2} \tag{5}$$

2) AIR GAP FLUX DENSITY WAVEFORM WITH THE INCORPORATION OF THE MOVER PERMEANCE FUNCTION

Following the prediction of B_{max}, a preliminary waveform of the spatial repartition of the flux density is admitted. It has the trapezoidal waveform illustrated in Fig. 8.

$B_t(z)$ is formulated in terms of the axial position z along the air gap as follows:

$$B_t(z) = \begin{cases} \dfrac{2B_{max}}{P_{io}} z & for\ 0 \le z \le \dfrac{P_{io}}{2} \\ B_{max} & for\ \dfrac{P_{io}}{2} \le z \le \tau_p - \dfrac{P_{io}}{2} \\ -\dfrac{2B_{max}}{P_{io}} z + \widehat{B} & for\ \tau_p - \dfrac{P_{io}}{2} \le z \le \tau_p + \dfrac{P_{io}}{2} \\ -B_{max} & for\ \tau_p + \dfrac{P_{io}}{2} \le z \le 2\tau_p - \dfrac{P_{io}}{2} \\ \dfrac{2B_{max}}{P_{io}} z - 2\widehat{B} & for\ 2\tau_p - \dfrac{P_{io}}{2} \le z \le 2\tau_p \end{cases} \tag{6}$$

where:

$$\begin{cases} P_{io} = \tau_p - Ps_{ow} \\ \widehat{B} = 2B_{max}\left(1 + \dfrac{Ps_{ow}}{P_{io}}\right) \end{cases} \tag{7}$$

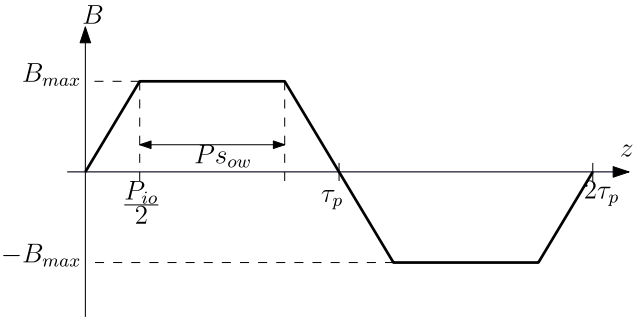

FIGURE 8. Air gap flux density trapezoidal waveform.

From a physical point of view, the variation of the air gap flux density between two adjacent poles is far from being linear. It is affected by the mover permeance variation. Indeed, accounting for the fact that $\mu_{PM} \ll \mu_{iron}$, the IPM topology is characterized by a remarkable variation of the mover permeance.

For the sake of a better representativeness of the predicted air gap flux density waveform, a permeance function related to the mover permeance variation is incorporated in the formulation of $B_t(z)$ as developed hereunder.

Within a radial position corresponding to the middle of the air gap, the mover permeance function has been inspired from the one adopted in [38] and in [39], where the stator slotting effect has been treated in the case of a rotating machine, and in the case of a linear one, respectively.

Assuming that the PM relative permeability is almost equal to the air one ($\mu_{PM} \simeq \mu_{air}$) with regards to μ_{iron}, an analogy between the stator slots and the mover magnetic circuit with the IPM arrangement has been considered. Accounting for this analogy, the slot opening and pitch in the conventional permeance function are substituted by the distance between adjacent pole shoes and the pole pitch, respectively. Doing so, the mover permeance function λ_m is expressed as:

$$\lambda_m(z) = \begin{cases} 1 - \beta\left(1 + \cos\dfrac{z}{0.8\,P_{io}}\pi\right) & for\ 0 \le z \le 0.8P_{io} \\ 1 & for\ 0.8P_{io} \le z \le \dfrac{\tau_p}{2} \end{cases} \tag{8}$$

where β is defined as:

$$\beta = \frac{1}{2}\left(1 - \frac{1}{\sqrt{1 - \left(\frac{P_{io}}{2g}\right)^2 (1+\nu^2)}}\right) \tag{9}$$

and where ν fulfills the following equation:

$$\frac{\pi}{P_{io}} y_m = \frac{1}{2}\ln\left(\frac{\sqrt{a_m^2+\nu^2}+\nu}{\sqrt{a_m^2+\nu^2}-\nu}\right) + \frac{2g}{P_{io}}\arctan\left(\frac{2g}{P_{io}}\frac{\nu}{\sqrt{a_m^2+\nu^2}}\right) \tag{10}$$

with:

$$\begin{cases} a_m = \sqrt{1 - \left(\dfrac{P_{io}}{2g_m}\right)^2} \\ y_m = \left(\dfrac{2K_m - 1}{2}\right) g \end{cases} \tag{11}$$

where g_m and K_m are a corrected air gap and a correction coefficient, respectively. These are expressed as follows:

$$\begin{cases} g_m = K_m g \\ K_m = \dfrac{\tau_p}{\tau_p - \xi_m g} \end{cases} \tag{12}$$

where ξ_m is expressed in terms of g, the mover pole pitch τ_p and the inter pole opening P_{io} as follows:

$$\xi_m = \frac{4}{\pi}\left(\frac{P_{io}}{2g}\arctan\left[\frac{P_{io}}{2g}\right] - \ln\left[\sqrt{1 + \left(\frac{P_{io}}{2g}\right)^2}\right]\right) \tag{13}$$

The total mover permeance function $\lambda_M(z)$ could be predicted using the symmetry for the second half of the north pole, and the duplicate for the south one, as depicted in Fig. 6(c). Taking the rotor permeance function into account, the air gap flux density turns to be $B_g(z)$ which is expressed as:

$$B_g(z) = \lambda_M(z) B_t(z) \tag{14}$$

3) PREDICTION OF THE BACK-EMF

Following the prediction of the air gap flux density, one can formulate the phase flux linkage and then deduce the back-EMFs induced in he armature phases. In order to improve the accuracy, the slotting effect within the stator should be taken into consideration. To do so, a stator permeance function λ_s is introduced. Similar to the mover one, λ_s is expressed in the middle of the air gap as:

$$\lambda_s(z) = \begin{cases} \dfrac{\mu_0}{g_c}\left[1 - \beta\left(1 + \cos\dfrac{z}{0.8s_0}\pi\right)\right] & \text{for } 0 \le z \le 0.8s_0 \\ \dfrac{\mu_0}{g_c} & \text{for } 0.8s_0 \le z \le \dfrac{\tau_s}{2} \end{cases} \tag{15}$$

where s_o and τ_s are the stator slot opening and pitch, respectively, and where g_c is the stator corrected air gap which is expressed in terms of the *Cater* factor. These are predicted in the same manner as g_m and K_m by substituting τ_p and P_{io} by τ_s and s_o, respectively. β is predicted using equation (9).

Following the determination of the stator permeance function along a half of stator slot, its multiplication enables the prediction of the permeance function for all the stator length λ_S according to the stator slots number. Doing so, the slotted machine air gap flux density could be expressed as:

$$B_{gs}(z) = \lambda_S(z) B_g(z) \tag{16}$$

Let us consider a coil of N_c turns. The flux linkage φ_c crossing the coil is expressed as:

$$\varphi_c = N_c \int_{z=0}^{z=\tau_s} 2\pi R_{is} B_{gs}(z) dz \tag{17}$$

where R_{is} is the inner stator radius.

The back-EMF induced in the coil is predicted as follows:

$$E_c = -\frac{d\varphi_c}{dt} \tag{18}$$

The phase back-EMF is predicted by adding the back-EMFs induced in the coils assigned to the phase which are identified using the star of slots approach [40], [41].

4) PREDICTION OF THE COGGING FORCE

Assuming an infinite length machine, the end effect turns to be null. The *Ns* teeth of the stator has the same shape. Consequently, the prediction of the cogging forces applied to the *Ns* teeth considers the same geometrical parameters. The cogging force F_g is the sum of the forces applied to the N_s teeth of the stator, as [39]:

$$F_g = \sum_{i=1}^{N_s} F_{gi} \tag{19}$$

where F_{gi} is the force applied to the i^{th} stator teeth which is expressed as followss

$$F_g(i) = 2\pi^2 R_s \left(\frac{s_o}{2}\right)\left(\frac{B_{tu}^2(i) - B_{tl}^2(i)}{2\mu_0}\right) \tag{20}$$

where $B_{tu}(i)$ and $B_{tl}(i)$ are the flux densities at the i^{th} tooth shoes upper and lower surfaces, respectively, and where R_s is the stator air gap radius including the tooth shoes width W_{ts}, such that:

$$R_s = R_{is} + W_{ts} \tag{21}$$

C. NUMERICAL PROCEDURE

A numerical procedure dedicated to the resolution of the proposed approach, has been developed. Its flowchart is illustrated in Fig. 9.

Moreover, and referring to its flowchart, the developed procedure enables:

- the prediction of the no-load features,
- the application of the proposed approach to the sizing of the mover pole shoe that will be treated hereunder.

IV. INVESTIGATION OF THE MOVER GEOMETRY

The proposed approach developed in the previous section is applied to the investigation of the impact of the pole shoe geometry on the IPM TLSM no-load air gap flux density for $r = M_{or} + \frac{g}{2}$. The investigation of the mover geometry has been achieved considering the rectangular and trapezoidal pole shoes described in section II.

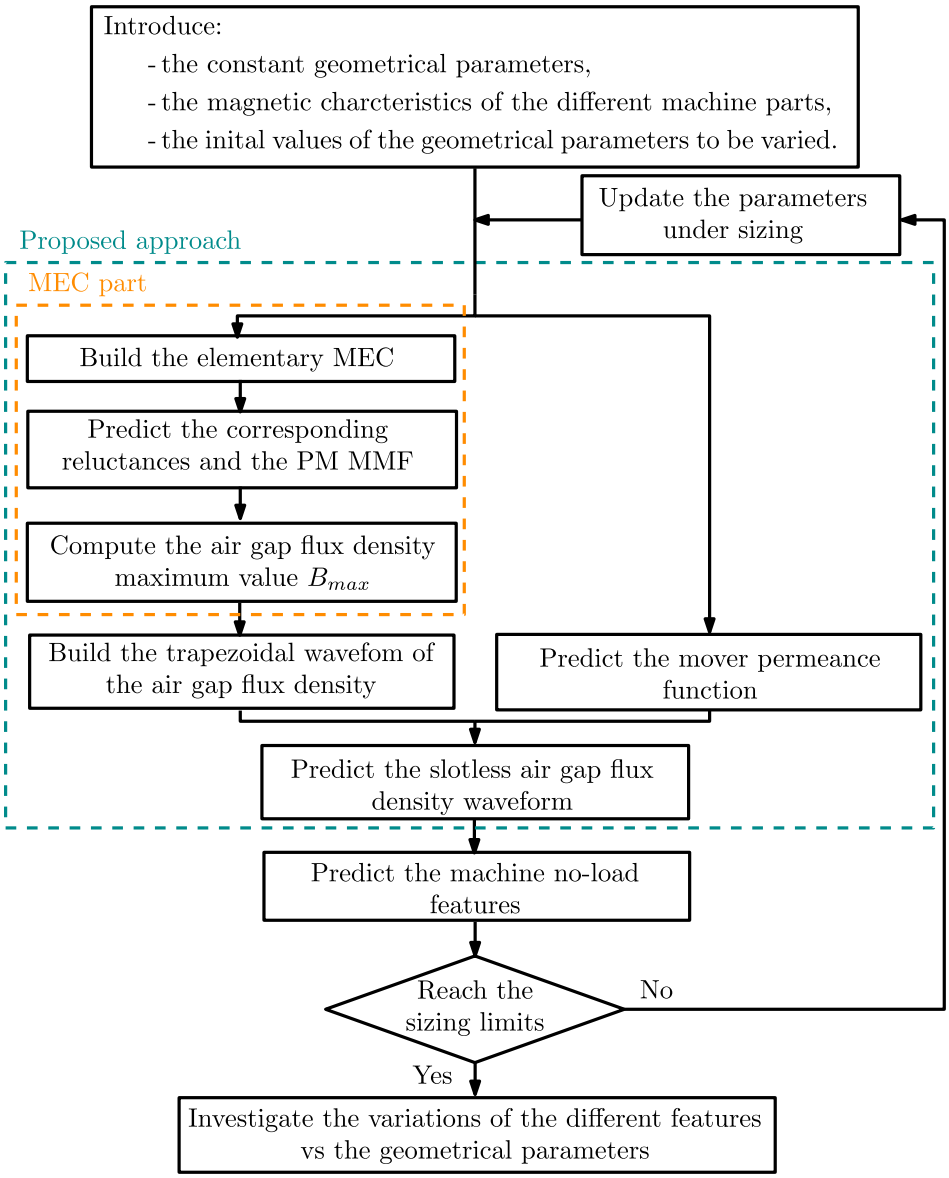

FIGURE 9. Flowchart of the numerical procedure enabling the resolution of the proposed approach and its application to the sizing of the mover pole shoe

A. CASE OF RECTANGULAR POLE SHOES

Figs. 10, 11, and 12 show the variations of the air gap flux density maximum value, fundamental amplitude, and THD, respectively, versus ratios R_{pw} and R_{psw}.

From the analysis of Figs. 10, 11, and 12, one can notice the following remarks:

- the maximum value of the air gap flux density grows with the decrease of R_{pw} which is allied to an increase of the PM axial length τ_{PM},
- for a given R_{pw}, the maximum value of the air gap flux density is reduced with the increase of R_{psw} which is associated to an increase of the pole shoes surface facing the air gap while the flux per pole is kept constant,
- there is a set of combinations (R_{pw}, R_{psw}) achieving a minimum air gap flux density THD, not exceeding 14.5%.

B. CASE OF TRAPEZOIDAL POLE SHOES

The developed analytical approach has been applied to the investigation of the effects of γ and R_{psw}, while keeping constant the value of R_{pw} (40%). The selection of this later is motivated by a compromise of the three features investigated in the case or rectangular pole shoes. The obtained results are shown in Figs. 13, 14, and 15 which illustrate the variations of the air gap flux density maximum value, fundamental harmonic amplitude, and THD, respectively.

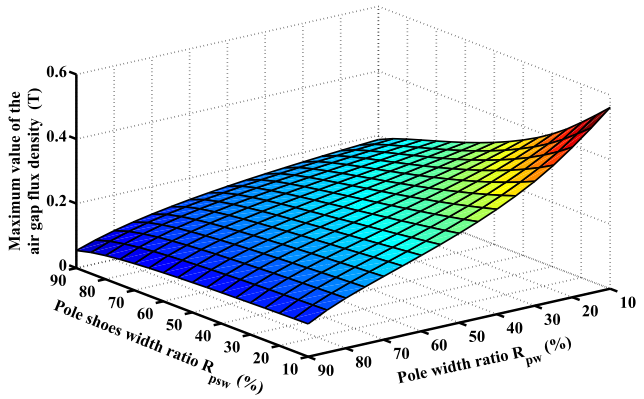

FIGURE 10. Air gap flux density maximum value vs. ratios R_{pw} and R_{psw}.

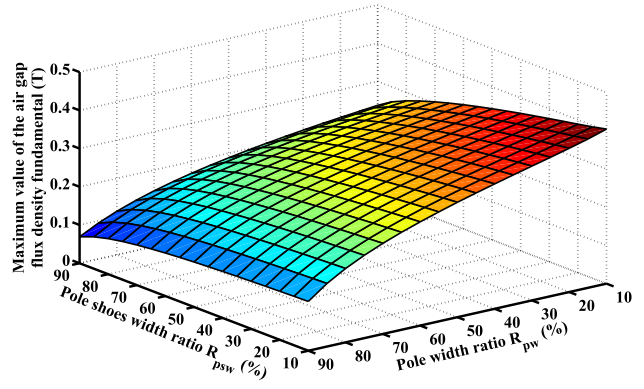

FIGURE 11. Amplitude of the air gap flux density fundamental harmonic vs. ratios R_{pw} and R_{psw}.

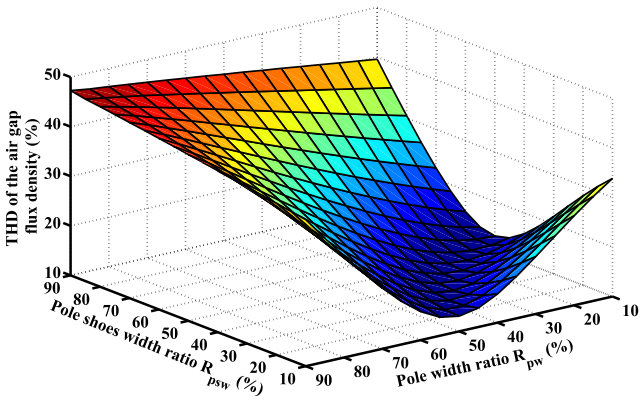

FIGURE 12. THD of the air gap flux density vs. ratios R_{pw} and R_{psw}.

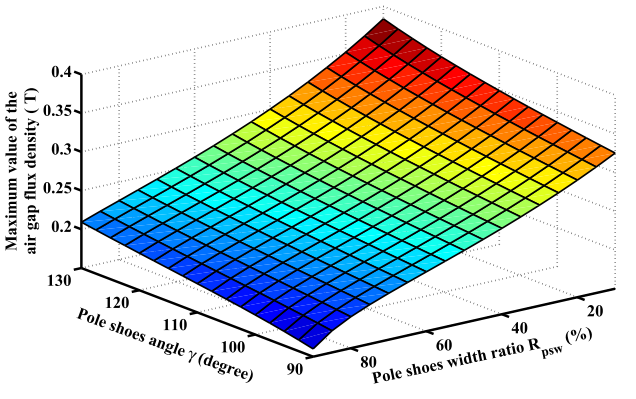

FIGURE 13. Air gap flux density maximum value vs. angle γ and ratio R_{psw}.

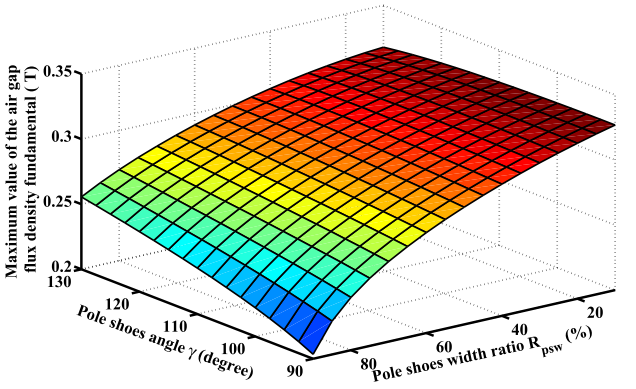

FIGURE 14. Amplitude of the air gap flux density fundamental harmonic vs. angle γ and ratio R_{psw}.

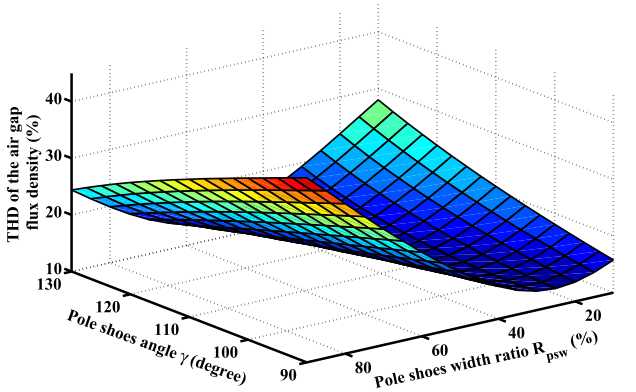

FIGURE 15. THD of the air gap flux density vs. angle γ and ratio R_{psw}.

Referring to Figs. 13, 14, and 15, one can notice that:

- for a given pole shoes width ratio R_{psw}, the air gap flux density maximum value B_{max} grows almost linearly with the increase of the pole shoes angle γ starting from 90° corresponding to rectangular pole shoes. The increase of B_{max} is allied to a decrease of the pole shoes surface facing the air gap while the flux per pole is kept constant,
- a similar behavior of the air gap flux density fundamental harmonic amplitude with regard to the pole shoes angle γ under constant pole shoes width ratio R_{psw} is noticed. With the decrease of R_{psw}, the increase of the air gap flux density fundamental harmonic amplitude with γ turns to be damped before its reversal to become a decrease for R_{psw} lower than 20%,
- in the manner of the rectangular pole shoes, there is a set of combinations (γ, R_{psw}) enabling a reduction of the harmonic content of the air gap flux density. Indeed,

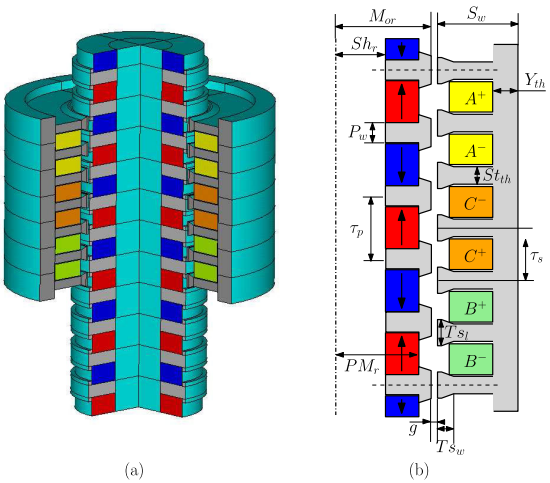

FIGURE 16. Selected IPM T-LSM. Legend: (a) 3D view, (b) basic concept.

TABLE 1. Selected IPM T-LSM main geometrical parameters.

Parameter	Symbol	Value (mm)
Mover outer radius	M_{or}	47.65
Shaft radius	Sh_r	22.25
Pole pitch	τ_p	21.6
Pole width	P_w	8.6
Air gap	g	1.5
Slot pitch	τ_s	18
Stator width	S_w	45.5
Yoke thickness	Y_{th}	14
Stator tooth thickness	St_{th}	6
Tooth shoes length	Ts_l	9.6
Tooth shoes width	Ts_w	6.45

a minimum THD of 13% is reached for the combination (γ=100°, R_{psw}=40%).

V. SELECTED MACHINE FEATURE INVESTIGATION

A. TOPOLOGYCAL DESCRIPTION

The selected IPM T-LSM has the topology shown in Fig. 16, where the main geometrical parameters are identified. These are listed in Table 1. The machine is equipped with:

- three phases inserted in six slots in the armature,
- five active trapezoidal-shaped poles achieved by spoke-type arranged ferrite PMs in the mover.

yielding a slot per pole and per phase equal to 2/5. The armature winding arrangement has been carried out applying the star of slots approach.

Following the pole shoe sizing procedure previously-treated, the combination (R_{pw}=40%, R_{psw}=40%, γ=100°) has been selected in so far as it fulfills the trade-off: high amplitudes of the flux density and of its fundamental component and low value of its THD.

B. ANALYTICAL AND FEA CHARACTERIZATION

The prediction of the no-load air gap flux density of the IPM T-LSM under study has been carried out using the proposed

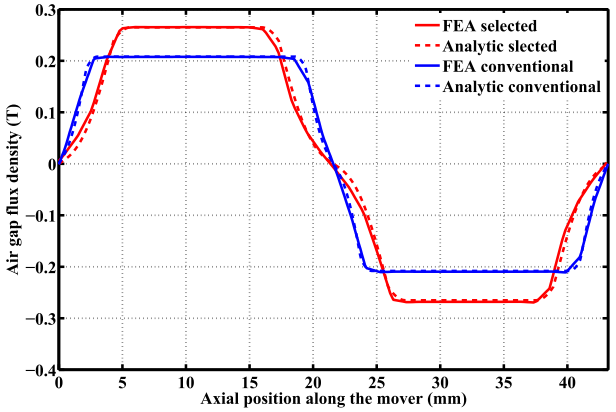

FIGURE 17. No-load air gap flux density waveforms of the selected (γ=100°) and conventional (γ=90°) IPM T-LSMs.

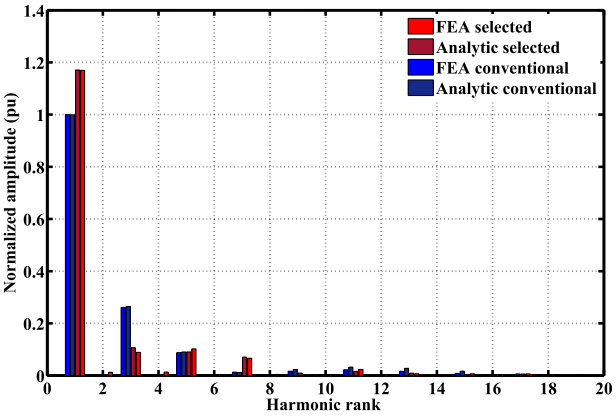

FIGURE 18. Spectra of the no-load air gap flux density waveforms of the selected (γ=100°) and conventional (γ=90°) IPM T-LSMs.

approach for $r = M_{or} + \frac{g}{2}$. It has led to the waveform shown in Fig. 17. The latter also includes the no-load air gap flux density waveform of the conventional topology characterized by rectangular pole shoes (γ=90°) and by (R_{pw}=50%, R_{psw}=40%). For the sake of validation, Fig. 17 shows the respective no-load air gap flux density waveforms yielded by 2D FEA.

The comparison between the trapezoidal and rectangular pole shoe geometries has been extended to the harmonic content of the air gap flux density which is characterized by the spectra shown in Fig. 18, where the amplitudes have been normalized to the fundamental one of the air gap flux density yielded by FEA characterizing the conventional topology.

From the analysis of Figs. 17 and 18, one can remark the following:

- the superiority of the selected topology over the conventional one regarding the harmonic content reduction,
- the good agreement between analytical and FEA results.

Moreover, the postprocessing of the FEA results has enabled the prediction of the no-load flux density mapping and lines which are illustrated in Fig 19. One can notice that the mover pole shoes are far from being saturated with a maximum flux density not exceeding 0.76T which is expected as far as ferrite PMs are used.

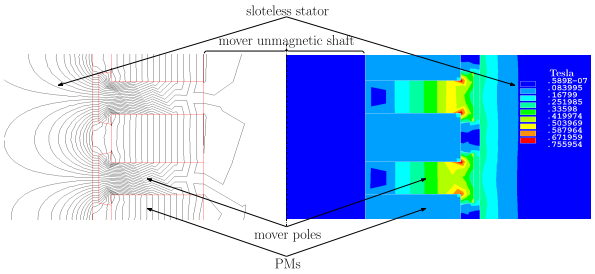

FIGURE 19. FEA-based characterization of the flux in a two pole axial cross-section of the selected IPM T-LSM concept. **Legend:** (left) flux lines distribution, (right) flux density mapping.

TABLE 2. THD and amplitude of the fundamental harmonic of the air gap flux density.

	conventional topology: R_{pw}=50% R_{pw}=40% γ=90°		selected topology: R_{psw}=60% R_{psw}=40% γ=100°	
	THD(%)	B_1(T)	THD(%)	B_1(T)
analytical results	28.5339	0.2578	14.7623	0.3017
2D FEA results	27.8092	0.2580	13.22	0.3026

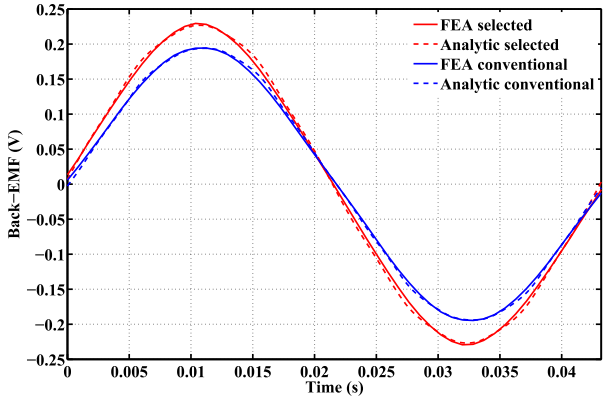

FIGURE 20. Back-EMFs of the selected (γ=100°) and conventional (γ=90°) IPM T-LSMs for unity-turn coils in the armature and a velocity $v = 1m/s$.

The effectiveness of the proposed approach is further confirmed by the values of the THDs of the conventional and selected topologies air gap flux densities yielded by the analytical and FEA models. These are provided in table 2.

Furthermore, the back-EMFs have been deduced from the predicted air gap flux densities according to the formulation given in paragraph III-B3. The obtained results are shown in Fig. 20. These results have been validated by a multi-static 2D FEA. This latter has been selected in so far as it is in harmony with the numerical procedure aimed at the resolution of the proposed analytical approach.

Finally, the cogging force have been calculated from the predicted air gap flux densities according to the formulation given in paragraph III-B4. The obtained results are shown in Fig. 21. These results have been validated by

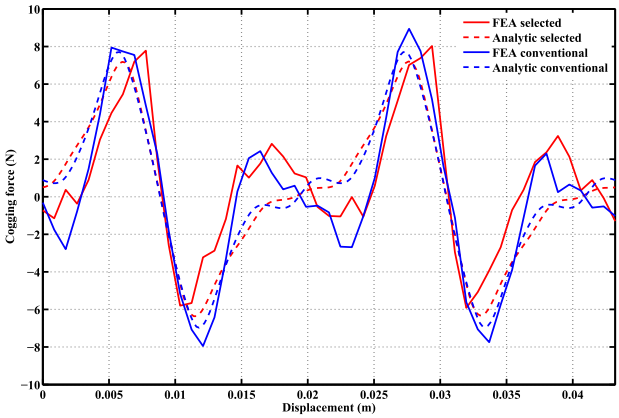

FIGURE 21. Cogging forces of the selected and conventional IPM T-LSMs.

TABLE 3. IPM T-LSM Prototype design parameters.

Parameter	Symbol	Value
Number of phases	q	3
Number of coils per phase	N_p	2
Number of turns per coil	N_c	380
Slot fill factor	K_f	0.675
Total number of mover poles	$2p_t$	8
Number of mover active poles	$2p$	5
PM remanence	B_r	0.18T
PM coercivity	H_c	147kA/m
Maximum stroke	S_M	65mm

a multi-static 2D FEA. Once again, the superiority of the selected topology over the conventional one is confirmed.

Beyond its accuracy, the proposed model offers a lower CPU time than the FEA one. Indeed, considering the prediction of the back-EMF of the selected topology, the resolution of the proposed model took 5.4219s. However, the one of the 2D FEA model, considering a multi-static behaviour and a number of element equal to 18206, reached up 470.40625s. For the sake of a better accuracy, the prediction of the back-EMF should be carried out considering a transient 2D FEA. Doing so, the FEA model turned to be complicated and its resolution required 9388.26s. The obtained results are suitably-adapted to the following experimental validation.

C. EXPERIMENTAL VALIDATION

The IPM T-LSM characterized by the combination (R_{pw}=40%, R_{psw}=40%, γ=100°) has been prototyped. It has a solid magnetic circuit made up of XC45 and has the design parameters listed in table 3. A photo of its stator and mover is given in Fig. 22(a). The prototyped IPM T-LSM is driven by a prime mover consisting in a separately-excited DC motor mechanically-coupled to a crank-rod system, as illustrated in Fig. 22(b) that gives a photo of the developed test bench.

An experimental test has been carried out under no-load generator operation. The waveform of the measured back-EMF at a mean speed of 0.25m/s is given in Fig. 23. Moreover, a transient 2D FEA carried out for a speed

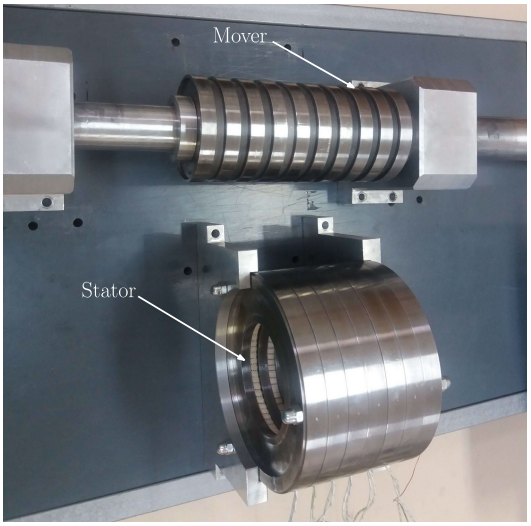

(a)

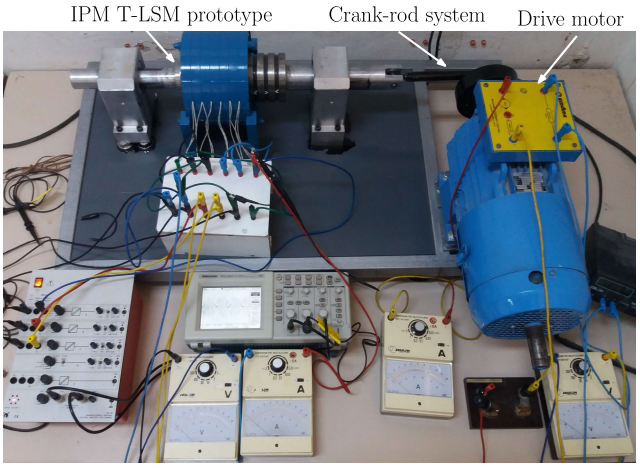

(b)

FIGURE 22. Experimental validation. **Legend: (a) Stator and mover of the prototyped machine, (b) Developed test bench.**

of 0.25m/s has enabled the prediction of the back-EMFs induced in the armature phases. One of the computed back-EMFs has been plotted in Fig. 23. For the sake of comparison, the back-EMF has been predicted by the proposed model under the same conditions (the number of turns per coil 380 and a linear speed of 0.25m/s).

One can notice that the transient FEA and experimental results are in harmony. The differences between the back-EMF waveforms are due to the relatively short stroke of the prototyped machine that amplifies the end effect. In spite of its simplicity, the proposed analytical model has led to a quite acceptable agreement with the experimental results.

The experimental investigation has been extended to the on-load operation of the prototyped IPM T-LSM used as a generator feeding a variable resistor and driven at a mean mover speed of 0.278m/s. The resulting load characteristic is

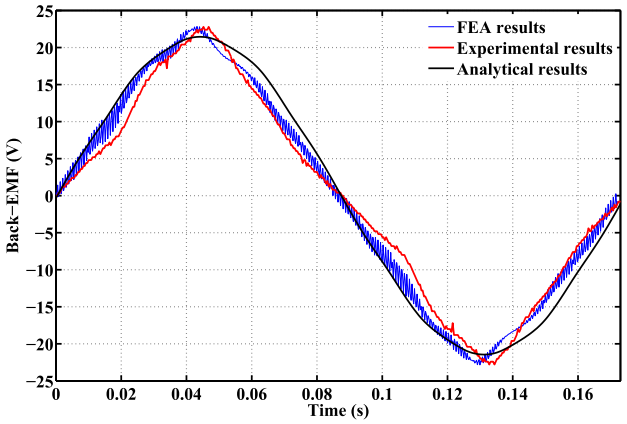

FIGURE 23. Back-EMF waveform for a mean speed of the mover of 0.25m/s.

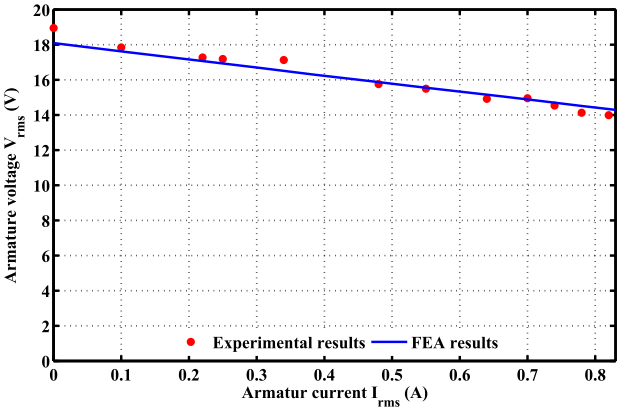

FIGURE 24. Load characteristic under generator operation with a variable resistor in the armature and for a mean speed of the mover of 0.278m/s.

shown in Fig. 24. This latter also illustrates the characteristic predicted by 2D FEA. One can notice a good agreement between FEA and experimental results.

The analytical prediction of the load characteristic is not feasible as far as the proposed model considers the no-load operation. To account for the armature magnetic reaction, one has to consider the total MEC incorporating the mover position variation. This would lead to a complicated model especially with the fractional-slot armature distribution.

VI. CONCLUSION

The paper proposed an approach to investigate the effects of pole shoe geometry on the no-load features of IPM T-LSMs. The introduced approach considers a two step procedure, as:

- the prediction of the maximum value of the air gap flux density using a simple MEC of an elementary section of the machine,
- the formulation of the flux density spatial repartition according to a trapezoidal waveform modulated by a mover permeance function.

Then, the proposed approach has been applied to the investigation of the impact of the mover geometry on the no-load

air gap flux density, considering both cases of rectangular and trapezoidal pole shoes. It has been shown that IPM T-LSMs equipped with trapezoidal pole shoes exhibit an air gap flux density with a relatively better quality. The developed sizing procedure enabled the selection of an IPM T-LSM with trapezoidal pole shoes. Its no-load air gap flux density, back-EMF, and cogging force have been predicted by the proposed analytical model and has been validated by 2D FEA. In order to highlight the superiority of the selected machine, its no-load features have been compared to the ones exhibited by the conventional topology equipped with rectangular pole shoes. A prototype of the selected machine has been built and tested under no- and on-load operation. The measured back-EMF waveform has been compared to the ones predicted by the proposed model and by the FEA one. It has been found that the experimental and FEA results are in harmony. The differences between the analytical and experimental results are due to the relatively short stroke of the prototyped machine that amplifies the end effect.

The proposed analytical approach could be extended to the prediction of the on-load features considering selected positions of the mover. Nevertheless, such an extension would inevitably compromise the simplicity of the proposed approach in so far as the armature magnetic reaction is far from being sinusoidal in the case of fractional-slot PM synchronous machines.

REFERENCES

[1] M. Chen, L. Huang, P. Tan, Y. Li, G. Ahmad, and M. Hu, "A stator-PM transverse flux permanent magnet linear generator for direct drive wave energy converter," *IEEE Access*, vol. 9, pp. 9949–9957, 2021.

[2] A. Musolino, M. Raugi, R. Rizzo, and L. Sani, "A semi-anaytical model for the analysis of a permanent magnet tubular linear generator," *IEEE Trans. Ind. Appl.*, vol. 54, no. 1, pp. 204–212, Jan. 2018.

[3] J. Du, D. Liang, and X. Liu, "Performance analysis of a mutually coupled linear switched reluctance machine for direct-drive wave energy conversions," *IEEE Trans. Magn.*, vol. 53, no. 9, pp. 1–10, Sep. 2017.

[4] L. Cappelli, F. Marignetti, G. Mattiazzo, E. Giorcelli, G. Bracco, S. Carbone, and C. Attaianese, "Linear tubular permanent-magnet generators for the inertial sea wave energy converter," *IEEE Trans. Ind. Appl.*, vol. 50, no. 3, pp. 1817–1828, May/Jun. 2014.

[5] S. Ding, W. Han, J. Sun, F. Jiang, G. Deng, and Y. Shi, "Modeling and analysis of a linear generator for high speed maglev train," *IEEE Access*, vol. 9, pp. 24637–24645, 2021.

[6] H. Wang, J. Li, R. Qu, J. Lai, H. Huang, and H. Liu, "Study on high efficiency permanent magnet linear synchronous motor for maglev," *IEEE Trans. Appl. Supercond.*, vol. 28, no. 3, pp. 1–5, Apr. 2018.

[7] J.-H. Jeong, C.-W. Ha, J. Lim, and J.-Y. Choi, "Analysis and control of electromagnetic coupling effect of levitation and guidance systems for semi-high-speed maglev train considering current direction," *IEEE Trans. Magn.*, vol. 53, no. 6, pp. 1–4, Jun. 2017.

[8] X. Xu, Z. Sun, B. Du, and L. Ai, "Pole optimization and thrust ripple suppression of new Halbach consequent-pole PMLSM for ropeless elevator propulsion," *IEEE Access*, vol. 8, pp. 62042–62052, 2020.

[9] S.-G. Lee, S.-A. Kim, S. Saha, Y.-W. Zhu, and Y.-H. Cho, "Optimal structure design for minimizing detent force of PMLSM for a ropeless elevator," *IEEE Trans. Magn.*, vol. 50, no. 1, pp. 1–4, Jan. 2014.

[10] C.-T. Liu, W.-P. Lin, C.-Y. Hung, and C.-C. Hwang, "Feasibility assessments and designs of a hybrid suspension system for motorbike application," *IEEE Trans. Ind. Appl.*, vol. 53, no. 4, pp. 3420–3427, Jul. 2017.

[11] E. Asadi, R. Ribeiro, M. B. Khamesee, and A. Khajepour, "Analysis, prototyping, and experimental characterization of an adaptive hybrid electromagnetic damper for automotive suspension systems," *IEEE Trans. Veh. Technol.*, vol. 66, no. 5, pp. 3703–3713, May 2017.

[12] Y. Sun, Z. Xu, Q. Zhang, and L. Liu, "A plate moving-magnet linear generator designed for free-piston engines," *IEEE Access*, vol. 8, pp. 75135–75144, 2020.

[13] L. Yang, Z. Xu, L. Liu, N. Liu, and H. Yu, "A tubular PM linear generator with a coreless moving-coil for free-piston engines," *IEEE Trans. Energy Convers.*, vol. 34, no. 3, pp. 1309–1316, Sep. 2019.

[14] M. W. Zouaghi, I. Abdennadher, and A. Masmoudi, "No-load features of T-LSMs with quasi-Halbach magnets: Application to free piston engines," *IEEE Trans. Energy Convers.*, vol. 31, no. 4, pp. 1591–1600, Dec. 2016.

[15] T. T. Dang, M. Ruellan, L. Prévond, H. B. Ahmed, and B. Multon, "Sizing optimization of tubular linear induction generator and its possible application in high acceleration free-piston stirling microcogeneration," *IEEE Trans. Ind. Appl.*, vol. 51, no. 5, pp. 3716–3733, Sep./Oct. 2015.

[16] A. Souissi, I. Abdennadher, and A. Masmoudi, *Linear Synchronous Machines: Application to Sustainable Energy and Mobility*. Singapore: Springer, 2019.

[17] S. Schneider, F. Rinderknecht, and H. E. Friedrich, "Design of future concepts and variants of the free piston linear generator," in *Proc. 9th Int. Conf. Ecological Vehicles Renew. Energies (EVER)*, Monte-calo, Monaco, Mar. 2014.

[18] C. Lu, S. Ferrari, and G. Pellegrino, "Two design procedures for PM synchronous machines for electric powertrains," *IEEE Trans. Transport. Electrific.*, vol. 3, no. 1, pp. 98–107, Mar. 2017.

[19] A. Souissi, M. W. Zouaghi, I. Abdennadher, and A. Masmoudi, "MEC-based modeling and sizing of a tubular linear PM synchronous machine," *IEEE Trans. Ind. Appl.*, vol. 51, no. 3, pp. 2181–2194, May 2015.

[20] H. Yang, Y. Li, H. Lin, Z. Q. Zhu, and S. Lyu, "Principle investigation and performance comparison of consequent-pole switched flux PM machines," *IEEE Trans. Transport. Electrific.*, vol. 7, no. 2, pp. 766–778, Jun. 2021.

[21] S. G. Min, "Integrated design method of linear PM machines considering system specifications," *IEEE Trans. Transport. Electrific.*, vol. 7, no. 2, pp. 804–814, Jun. 2021.

[22] S.-H. Lee, I.-J. Yang, W.-H. Kim, and I.-S. Jang, "Electromagnetic vibration-prediction process in interior permanent magnet synchronous motors using an air gap relative permeance formula," *IEEE Access*, vol. 9, pp. 29271–29278, 2021.

[23] J. Zhang, H. Yu, M. Hu, L. Huang, and T. Xia, "Research on a PM slotless linear generator based on magnet field analysis model for wave energy conversion," *IEEE Trans. Magn.*, vol. 53, no. 11, pp. 1–4, Nov. 2017.

[24] Z. Song, C. Liu, K. Feng, H. Zhao, and J. Yu, "Field prediction and validation of a slotless segmented-Halbach permanent magnet synchronous machine for more electric aircraft," *IEEE Trans. Transport. Electrific.*, vol. 6, no. 4, pp. 1577–1591, Dec. 2020.

[25] A. Souissi, I. Abdennadher, R. D. Stefano, A. Masmoudi, and F. Marignetti, "Pole shapebased reduction of the harmonic content of the IPM T-LSM air gap flux density," *IEEE Trans. on Industrial Electronics*, vol. 65, no. 2, pp. 1429–1437, Feb. 2018.

[26] S. G. Min, G. Bramerdorfer, and B. Sarlioglu, "Analytical modeling and optimization for electromagnetic performances of fractional-slot PM brushless machines," *IEEE Trans. Ind. Electron.*, vol. 65, no. 5, pp. 4017–4027, May 2018.

[27] T. Wu, Z. Feng, C. Wu, G. Lei, Y. Guo, J. Zhu, and X. Wang, "Multi-objective optimization of a tubular coreless LPMSM based on adaptive multiobjective black hole algorithm," *IEEE Trans. Ind. Electron.*, vol. 67, no. 5, pp. 3901–3910, May 2020.

[28] P.-D. Pfister, X. Yin, and Y. Fang, "Slotted permanent-magnet machines: General analytical model of magnetic fields, torque, eddy currents, and permanent-magnet power losses including the diffusion effect," *IEEE Trans. Magn.*, vol. 52, no. 5, pp. 1–13, May 2016.

[29] P. Liang, F. Chai, Y. Li, and Y. Pei, "Analytical prediction of magnetic field distribution in spoke-type permanent-magnet synchronous machines accounting for bridge saturation and magnet shape," *IEEE Trans. Ind. Electron.*, vol. 64, no. 5, pp. 3479–3488, May 2017.

[30] Z. Djelloul-Khedda, K. Boughrara, F. Dubas, A. Kechroud, and B. Souleyman, "Semi-analytical magnetic field predicting in many structures of permanent-magnet synchronous machines considering the iron permeability," *IEEE Trans. Magn.*, vol. 54, no. 7, pp. 1–21, Jul. 2018.

[31] S. T. Boroujeni, S. P. Emami, and P. Jalali, "Analytical modeling of eccentric PM-inset machines with a slotless armature," *IEEE Trans. Energy Convers.*, vol. 34, no. 3, pp. 1466–1474, Sep. 2019.

[32] W. Ullah, F. Khan, E. Sulaiman, I. Sami, and J.-S. Ro, "Analytical subdomain model for magnetic field computation in segmented permanent magnet switched flux consequent pole machine," *IEEE Access*, vol. 9, pp. 3774–3783, 2021.

[33] X. Kong, Y. Hua, Z. Zhang, C. Wang, and Y. Liu, "Analytical modeling of high-torque-density spoke-type permanent magnet in-wheel motor accounting for rotor slot and eccentric magnetic pole," *IEEE Trans. Transport. Electrific.*, vol. 7, no. 4, pp. 2683–2693, Dec. 2021.
[34] W. Hu, X. Zhang, Y. Lei, Q. Du, L. Shi, and G. Liu, "Analytical model of air-gap field in hybrid excitation and interior permanent magnet machine for electric logistics vehicles," *IEEE Access*, vol. 8, pp. 148237–148249, 2020.
[35] A. Waheed and J.-S. Ro, "Analytical modeling for optimal rotor shape to design highly efficient line-start permanent magnet synchronous motor," *IEEE Access*, vol. 8, pp. 145672–145686, 2020.
[36] Z. Zhu, H. Zhu, X. Li, J. Zhu, and M. Cheng, "Dynamic equivalent magnetic network analysis of an axial PM bearingless flywheel machine," *IEEE Access*, vol. 9, pp. 32425–32435, 2021.
[37] D. Fu, J. Gong, Y. Xu, F. Gillon, and N. Bracikowski, "Coupled circuit and magnetic model for a transverse flux permanent magnet linear motor," *IEEE Access*, vol. 8, pp. 159274–159283, 2020.
[38] Z. Q. Zhu and D. Howe, "Instantaneous magnetic field distribution in brushless permanent magnet DC motors. III. Effect of stator slotting," *IEEE Trans. Magn.*, vol. 29, no. 1, pp. 143–151, Jan. 1993.
[39] A. Souissi, I. Abdennadher, and A. Masmoudi, "Analytical prediction of the no-load operation features of tubular-linear permanent magnet synchronous machines," *IEEE Trans. Magn.*, vol. 52, no. 1, pp. 1–7, Jan. 2016.
[40] N. Bianchi, S. Bolognani, and M. D. Pre, "Magnetic loading of fractional-slot three-phase PM motors with nonoverlapped coils," *IEEE Trans. Ind. Appl.*, vol. 44, no. 5, pp. 1513–1521, Sep./Oct. 2008.
[41] M. Barcaro, N. Bianchi, and F. Magnussen, "Six-phase supply feasibility using a PM fractional-slot dual winding machine," *IEEE Trans. Ind. Appl.*, vol. 47, no. 5, pp. 2042–2050, Sep./Oct. 2011.

AMAL SOUISSI received the B.S. degree in electromechanical engineering and the Ph.D. degree in electrical engineering from the Sfax Engineering National School (SENS), University of Sfax, Sfax, Tunisia, in 2014 and 2017, respectively.

She is currently a member of the Research Laboratory on Renewable Energies and Electric Vehicles (RELEV), University of Sfax, working on a postdoctoral project dealing with the design and control of a ropeless elevator equipped with a modular PM linear motor. Her research interests include the design, modelling, and sizing of tubular and flat linear PM synchronous machines.

IMEN ABDENNADHER received the B.S. degree in electromechanical engineering, the M.S. degree in electrical machine analysis and control, the Ph.D. degree, and the Postdoctoral Research Habilitation degree in electrical engineering from the Sfax Engineering National School (SENS), University of Sfax, Sfax, Tunisia, in 2005, 2006, 2012, and 2017, respectively.

In 2009, she joined the SENS as an Assistant Professor. Then, she has been promoted to the grade of an Associate Professor, in 2012. She is currently a Professor in electric power engineering and a member of the Research Laboratory on Renewable Energies and Electric Vehicles (RELEV), University of Sfax. Her research interests include the design, modelling, sizing, and optimization of rotating, and linear AC machines applied to sustainable development systems.

AHMED MASMOUDI (Senior Member, IEEE) received the B.S. degree from the Sfax Engineering National School (SENS), University of Sfax, Sfax, Tunisia, in 1984, the Ph.D. degree from Pierre and Marie Curie University, Paris, France, in 1994, and the Postdoctoral Research Habilitation degree from SENS, in 2001, all in electrical engineering.

In 1988, he joined Tunisian University, where he held different positions involved in both education and research activities. He is currently a Full Professor in electric power engineering with SENS. He is also the Head of the Research Laboratory on Renewable Energies and Electric Vehicles, and the Coordinator of the master on sustainable mobility actuators, including research and technology. He is the author of more than 100 papers, 26 among which are published in IEEE TRANSACTIONS. He is the author and coauthor of four books and the Co-Inventer of a U.S. patent. He has presented up to 11 keynote speeches in international conferences. His research interests include the design of new topologies of AC machines and the implementation of advanced and efficient control strategies in drives and generators, applied to automotive, and to renewable energy systems.

Prof. Masmoudi has been the Chair of the Program and Publication Committees of the International Conference on Ecological Vehicles and Renewable Energie (EVER), annually-organized in Monaco, since 2007. He is also the Chair of the Founding, the Technical Program, and the Publication Committees of the International Conference on Sustainable Mobility Applications, Renewables, and Technology (SMART) that has been organized in the Australian College of Kuwait, in November 2015, and will be organized remotely, in November 2022.